

High-stress fatigue crack propagation in thin AA2024-T3 sheet material

Eric Breitbarth¹  | Tobias Strohmann¹ | Guillermo Requena^{1,2}

¹Institute of Materials Research, German Aerospace Center (DLR), Cologne, 51147, Germany

²Metallic Structures and Materials Systems for Aerospace Engineering, RWTH Aachen University, Aachen, 52062, Germany

Correspondence

Eric Breitbarth, Institute of Materials Research, German Aerospace Center (DLR), Linder Hoehe, 51147 Cologne, Germany.
Email: eric.breitbarth@dlr.de

Funding information

German Federal Ministry for Economic Affairs and Energy (BMWi)

Abstract

Fatigue crack growth in 1.6-mm-thick sheets of aluminium alloy AA2024-T3 was investigated under very high-stress conditions using 950-mm-wide middle tension (MT) specimens. Experiments were conducted by applying uniaxial load ratios R (0.1, 0.3 and 0.5) with the maximum nominal stress of 120 MPa following conditions relevant for aircraft fuselage structures. The experiments were conducted with digital image correlation to determine loading conditions acting on the crack tip. Stable crack growth rates of up to $da/dN > 4$ mm/cycle and $\Delta K > 100$ MPa $\sqrt{\text{m}}$ were reached, and final crack lengths $2a > 500$ mm were obtained. High-stress intensity factors cause plastic zone sizes that extend up to approximately 100 mm from the crack tip. The da/dN - ΔK data obtained in this study provide crucial information about the fatigue crack growth and damage tolerance of very long cracks under high-stress conditions in thin lightweight structures.

KEYWORDS

crack tip loading, digital image correlation, fatigue crack growth, plastic zones

1 | INTRODUCTION

Structural assessment of aircraft fuselage structures in terms of fatigue and residual strength during their operational life is necessary to meet the safety requirements. This assessment covers the entire range from crack initiation to stable crack growth and final rupture. Fatigue cracks can have fast crack propagation rates in the last growth stage before final failure, and thus, this regime accounts for only a small part of the service life cycles. Nevertheless, this stage determines the damage tolerance properties of the structure as a whole. Therefore, profound knowledge of fatigue, fracture behaviour and potential failure modes of the used materials are required.^{1,2}

Aluminium alloys such as AA2024 (AlCu4Mg) are widely used for aircraft fuselage structures. Determination

of the damage tolerance of these alloys comprises several stages: (i) Fatigue life curves (S - N or Wöhler curves) provide information about crack initiation,³ while (ii) subsequent stable fatigue crack growth (FCG) is characterized by crack propagation curves (da/dN - ΔK) for small-scale yielding (SSY) conditions. For large-scale yielding (LSY) conditions in the presence of significant plasticity, the cyclic J integral is sometimes used instead of ΔK , although this requires complex information about the local nonlinear-elastic constitutive behaviour.^{4,5} Data is determined with standard compact tension (CT) or middle tension (MT) specimens up to a ΔK range of approximately 30 to 40 MPa $\sqrt{\text{m}}$.⁶⁻⁹ FCG in ductile materials is generally related to transgranular ductile striation formation¹⁰ with cyclic plastic deformations at the crack tip.¹¹ (iii) Final rupture and

This is an open access article under the terms of the Creative Commons Attribution License, which permits use, distribution and reproduction in any medium, provided the original work is properly cited.

© 2020 The Authors. Fatigue & Fracture of Engineering Materials & Structures published by John Wiley & Sons Ltd

residual strength are captured in terms of crack growth resistance curves ($J-\Delta a$ or $K_R-\Delta a$). Here, the specimen is loaded quasi-statically instead of cyclically so that the material tears slowly with large plastic deformations in the vicinity of the crack tip.¹² This last stage requires the use of specimens with widths greater than 600 mm to achieve K -values well above $100 \text{ MPa}\sqrt{\text{m}}$.^{13–15} Discrepancies in the size of the specimens required to investigate the transition from stable crack growth to the final rupture at very high stresses often leads to a gap in FCG curves typically available for AA2024, as FCG data for high-stress intensity factors are rarely available in the literature.

Recent advances in experimental mechanics have been achieved by the application of digital image correlation (DIC) in fracture mechanic experiments because full-field information about the displacements and strains provides access to the local crack tip field.^{16,17} Computational algorithms enable the determination of the J -integral and the stress intensity factors by exploiting the characteristic crack tip field^{18,19} or by using integration techniques.^{20–22} In addition, DIC shows features that influence the entire deformation field of the specimen, for example, the stress dead zone in the centre of MT specimens between the crack tips.²³ These are valuable methods for investigating crack propagation in more detail and for identifying relevant crack driving mechanisms.^{24–26}

This study presents a testing procedure to study the growth of long fatigue cracks in aluminium alloys subjected to very high-stress conditions to fill the gap between classical FCG data and stable crack extension. Centre-cracked specimens (950 mm wide) are used to investigate FCG in 1.6-mm-thick AA2024-T3 sheets at ΔK regimes beyond $100 \text{ MPa}\sqrt{\text{m}}$. The tests are supported by DIC to determine the stress intensity factors acting during the experiment based on the interaction integral. The FCG data can be used to estimate the lifetime of highly stressed fatigue cracks in aircraft fuselage structures.

2 | METHODOLOGY

2.1 | Material

The aluminium alloy AA2024-T3 (AlCu4Mg), which is widely used in the aircraft industry, is investigated in this study. The material was purchased from a commercial supplier in the form of 1.6-mm-thick rolled sheets. The supplier provided the following mechanical properties: Young's modulus $E = 71.4 \text{ GPa}$ and yield strength $\sigma_{\text{yield}} = 345 \text{ MPa}$.

2.2 | Experimental setup

The setup of the FCG experiments is shown in Figure 1. A standard uniaxial servo-hydraulic testing machine (1) with a digital controller and a load capacity of 400 kN was used; the AA2024-T3 specimens (2) have total dimensions of $1,250 \times 950 \times 1.6 \text{ mm}^3$ and are machined by water jet cutting. An initial notch with a length of $2a = 20 \text{ mm}$ is introduced at the centre of the specimen by a saw cut.

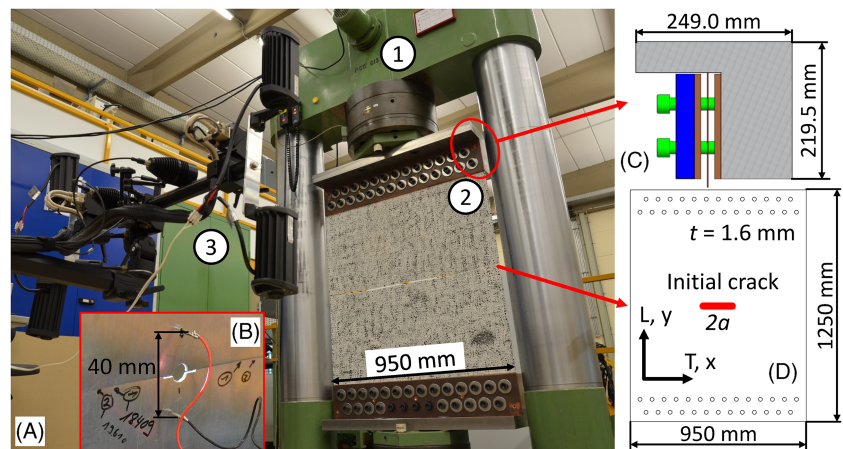
The crack length is determined using direct current potential drop (DCPD) during the experiment using Johnson's equation.²⁷ The voltage was measured between two pins at the centre of the specimen at a vertical distance of 40 mm to each other (Figure 1B). Massive copper plates in the clamping (brown parts in Figure 1C) were used to transmit electrical current to the specimen. The clamps were isolated from the machine to avoid alternative current paths. Owing to the large dimensions of the specimens, a relatively high constant current of 80 A (resulting in a voltage of $\sim 1 \text{ V}$) was necessary to obtain an adequate potential difference of approximately 0.14 mV for the initial 20-mm-long notch. The specimen is held by clamps in an area of $950 \times 170 \text{ mm}^2$ on each side and loaded parallel to its rolling direction, L . T denotes the transverse direction (Figure 1D).

A commercial 3D DIC system ((3) in Figure 1A; GOM Aramis 12M) was used to obtain the full-field displacement and strain information of the free surface of specimen ($950 \times 910 \text{ mm}^2$) during the experiment. The strains are given as the total strains ($\epsilon_{\text{total}} = \epsilon_{\text{elastic}} + \epsilon_{\text{plastic}}$), because no additional material model is included in the calculations. Two cameras with a focal length of 24 mm were positioned at a horizontal distance of 586 mm from each other. The entire gauge area was captured at a distance of approximately 1,550 mm. Six lamps illuminated the specimen during the test. For the DIC measurements, the specimens were painted white using a commercial water-based spray paint. Then, a black speckle pattern was generated by applying black acrylic paint with a brush onto the surface of the specimen. The DIC system had a spatial resolution of 4.8 mm (1 pixel = 0.32 mm) with a facet size of $19 \times 19 \text{ pixel}^2$ and a facet distance of 15 pixel.

2.3 | Experimental procedure

Three different loading conditions were analyzed during the FCG experiments, as shown in Figure 2. In each case, the maximum nominal stress σ_{max} was kept constant at 120 MPa with the maximum force $F_{\text{max}} = 182.4 \text{ kN}$; this corresponds to roughly one third of the yield stress. To

FIGURE 1 (a) Experimental setup: (1) servo-hydraulic testing machine, (2) mounted middle tension (MT) specimen and (3) commercial 3D digital image correlation system; (b) direct current potential drop measurement; (c) clamping of the specimen; and (d) sketch of the MT specimen [Colour figure can be viewed at wileyonlinelibrary.com]



test three different load ratios ($R = \sigma_{\min}/\sigma_{\max}$), the minimal force was increased from 0.1_{\max} to 0.3_{\max} and to 0.5_{\max} . The maximum stress intensity factors K_{\max} and the size of the primary plastic zone (PPZ) were expected to be constant because the maximal stresses remain constant. A trapezoidal waveform with a period of 4 s was selected to ensure that the specimen is always subjected to maximal load, even if the stiffness of the specimen decreases because of the increasing crack lengths. To ensure repeatability, the experiments were subsequently conducted under the exact same conditions following the standard ASTM E647-15.

The 3D DIC measurements were conducted automatically at the minimum and maximum loads whenever the crack length increased by Δa between 5 to 10 mm. A total of approximately 100 images were captured during each crack growth experiment.

Fatigue crack propagation curves ($da/dN-\Delta K$) were obtained using two different techniques for determining ΔK . In both cases, da/dN was calculated using the secant

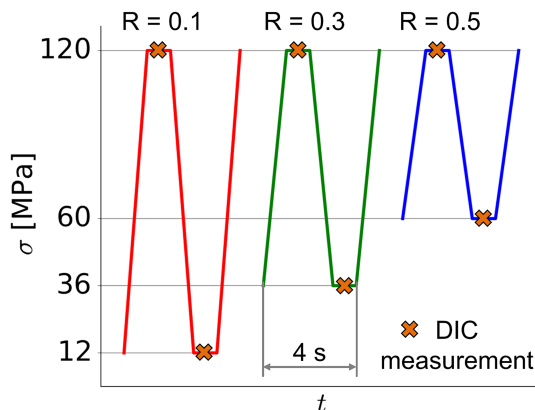


FIGURE 2 Details of the loading conditions during fatigue crack growth [Colour figure can be viewed at wileyonlinelibrary.com]

method according to ASTM E647-15. Then, ΔK was calculated using the linear-elastic finite element solution and with the DIC postprocessor based on the interaction integral.^{22,28,29} The interaction integral method was implemented in a Python postprocessor as a line integral as described in Breitbarth et al.³⁰ For DIC-based ΔK_{DIC} evaluation, DIC datasets with the minimum and maximum loads were used. In each dataset, 10 increasing integration paths were automatically defined outside the plastic zone at a distance of approximately 2 mm from each other at maximum load. Then, the same contours were used at the minimum loads. Finally, ΔK_{DIC} was calculated by subtracting the mean values at each load level. Predominant plane-stress conditions were expected because of the thin sheet material.

2.4 | Numerical analysis

3D finite element analysis (FEA) was used to calculate the stress intensity factors and investigate the primary and cyclic plastic zones. The simulations were set up as a parametric model with ANSYS parametric design language (APDL) in ANSYS Classic 19.1 and can be summarized as follows:

1. Stress intensity factors: free-mesh, crack tip element size = 0.5 mm, linear-elastic.
2. PPZ: free-mesh, increasing element size = 0.5 to 5 mm, elastic-plastic.
3. Cyclic plastic zone: mapped-mesh, element size = 1 mm, elastic-plastic.

The material tensile properties determined by standard tensile tests are shown in Figure 3. In the elastic region, the material model has a Young's modulus $E = 71.4$ GPa and a Poisson ratio $\nu = 0.33$. For the

elastic-plastic simulations of the plastic zone, a multi-linear isotropic hardening model (MISO) with a yield strength $\sigma_{\text{yield}} = 345 \text{ MPa}$ and nine data points indicated in Figure 3 (black circles) were used.

Considering symmetry conditions, only one fourth of the specimen was modelled to reduce computational effort (Figure 4). Linear eight node hexahedron (SOLID185) elements were selected as they provide a suitable trade-off between accuracy and computational time. The stress intensity factors (1) and PPZ sizes (2) were evaluated for increasing crack lengths between 50 mm and 350 mm in steps of $\Delta a = 5 \text{ mm}$. In these cases, a free mesh was used to mesh the surface area. The mesh size of the coarse part of the model outside the crack tip area was about 5 mm, with local refinements up to 0.5 mm in the vicinity of the crack tip. The 2D surface mesh was then extruded with four subdivisions in the thickness direction; the crack tip load K_I was calculated using the interaction integral provided in ANSYS via the CINT command³¹ by averaging the node values along the crack front.

For the simulation of the cyclic plastic zones (3), a regularly shaped mesh, that is, a mapped mesh, was necessary to ensure that all plastic zone elements have the same size and shape (Figure 4). The edge length in the refined region was 1.0 mm. The cyclic plastic zone was simulated for the three load ratios R (see Figure 2) at a crack length $a = 200 \text{ mm}$. A total of 30 load cycles (= 60 load steps) were calculated in each simulation according to the peak loads shown in Figure 2. The elements with changing plastic energy density between two following load steps were selected in postprocessing to reveal the

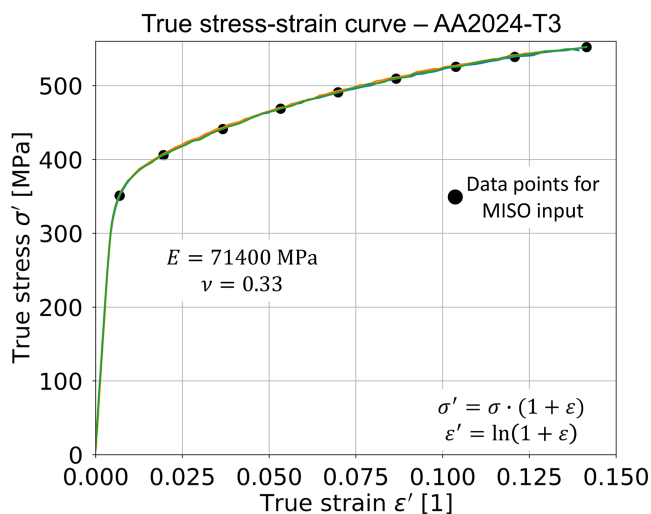


FIGURE 3 Tensile properties of the AA2024-T3 sheet material based on three tensile tests used for the multilinear isotropic hardening model (MISO) [Colour figure can be viewed at wileyonlinelibrary.com]

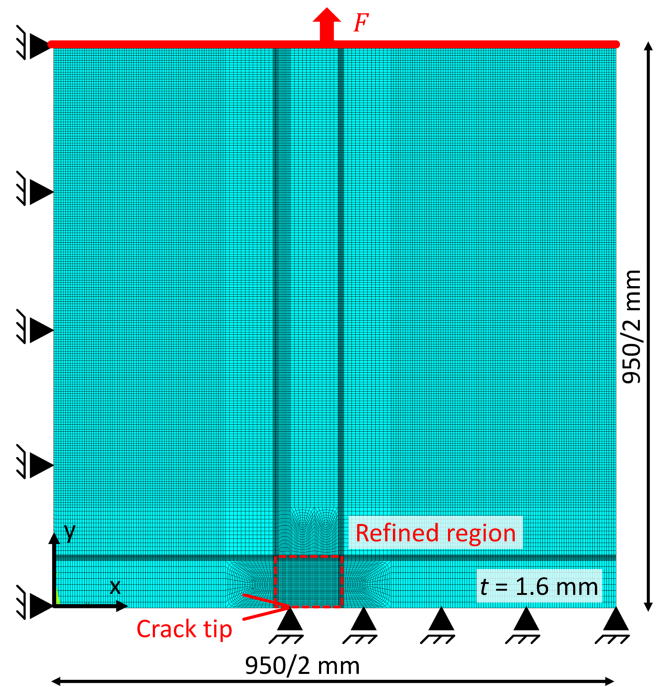


FIGURE 4 3D finite element model with boundary conditions and locally refined mapped mesh for the simulation of the cyclic plastic zone [Colour figure can be viewed at wileyonlinelibrary.com]

cyclic plastic zone. The details of this procedure can be found in Breitbarth and Besel.³²

2.5 | Fractography

The fracture surfaces were analyzed using a scanning electron microscope (Zeiss Ultra 55 FEG device) to reveal predominant crack growth mechanisms. The acceleration voltage was set at 15 kV. Samples of 50 mm length were cut from the tested specimens with a handsaw, cleaned by compressed air followed by cleaning under ethanol and distilled water.

3 | RESULTS

3.1 | PPZ and stress intensity factors

The size of the PPZs and stress intensity factors predicted by the finite element simulations are shown in Figure 5A,B, respectively. The surface shapes of the PPZs at different crack lengths are plotted in blue while the red dots indicate the crack tip positions. The red lines were fitted with a quadratic function to illustrate the overall boundaries of the growing crack. The crack tip load $K_{I,\text{max}}$ increases with increasing crack length to

values greater than $100 \text{ MPa}\sqrt{\text{m}}$ for crack lengths greater than 200 mm. Consequently, the corresponding elastic-plastic simulations predict very large PPZs that extend up to about 100 mm from the crack tip for a 325-mm-long crack. This is in good agreement with Irwin's PPZ size estimation $r_p = \frac{1}{\pi} \left(\frac{K_I}{\sigma_{\text{yield}}} \right)^2$ in the plane stress state.³³ Simulations for crack lengths $a \geq 325$ mm were aborted because of net-section yielding. The plastic zone transforms from a rounded shaped to a butterfly-like shape with increasing crack length.

Figure 6 shows a map of the von Mises equivalent stress σ_{eqv} obtained from the elastic plastic simulations for a crack length of $a = 250$ mm under maximum loading conditions. The PPZ is shown in grey, as the colour bar is limited to $R_{p0.2}$. Therefore, the DIC and FEA results are comparable.

3.2 | Experimental strain information

Figure 7 shows representative DIC strain fields for each of the three load ratios in terms of the von Mises equivalent strain $\varepsilon_{\text{eqv}} (= (2/3 \varepsilon_{ij} \varepsilon_{ij})^{1/2},^{34})$ right before the final fracture occurred. The DIC measurements shown in this figure are conducted under maximum load. In each case, the crack propagated symmetrically to the centre and it was almost perpendicular to the load axis. The overall strain distributions in the testing area are very similar for all specimens,

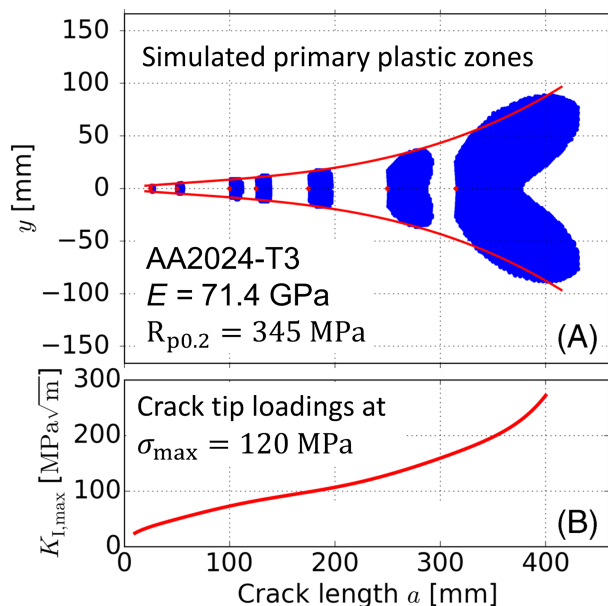


FIGURE 5 (A) Primary plastic zones on the surface based on finite element simulations at a nominal stress of 120 MPa and (B) estimated stress intensity factors [Colour figure can be viewed at [wileyonlinelibrary.com](https://onlinelibrary.com)]

as shown representatively in Figure 7A. Therefore, only the regions close to the crack tip are plotted for load ratios $R = 0.3$ and $R = 0.1$ in Figure 7B,C, respectively. The colour scale bar is limited to a maximum $\varepsilon_{\text{eqv}} = 0.68\%$ to reveal plastic deformation ($\varepsilon_{\text{eqv,yield}} = 0.2\% + R_{p0.2}/E = 0.2\% + 345 \text{ MPa}/71.4 \text{ GPa} = 0.68\%$). Thus, red areas in the vicinity of the crack tips indicate PPZs. The size of the PPZ is similar in the contour plots of the elastic-plastic simulation and the DIC measurement. However, the shapes of plastic zones differ because of the spatial resolution limits of the DIC system (comparing Figures 6 and 7).

The specimens with load ratios of 0.5, 0.3 and 0.1 finally failed because of the unstable fracture at crack lengths a of 277, 251 and 242 mm with maximum mode I stress intensity factors of 144, 130 and 122 $\text{MPa}\sqrt{\text{m}}$ and the load cycles of 36.6×10^3 , 21.2×10^3 and 17.2×10^3 , respectively. Thus, higher load ratios lead to a longer fatigue crack, and higher maximum stress intensity factors could be reached. Further, this leads to larger PPZs, as shown in Figure 7A-C. The crack extension for the $R = 0.5$ experiment reached about 96 mm. In this case, the length of the linear-elastic ligament is about 110 mm. Further, the strain fields show extensive strain redistributions throughout the tested area owing to the long crack: While the centre of the specimen is practically load-free (blue regions), the areas close to the lateral periphery of the specimen (green and yellow) are subjected to equivalent strains greater than 0.45%. A video showing the crack propagation and extension of the strain maps is provided in Video S1.

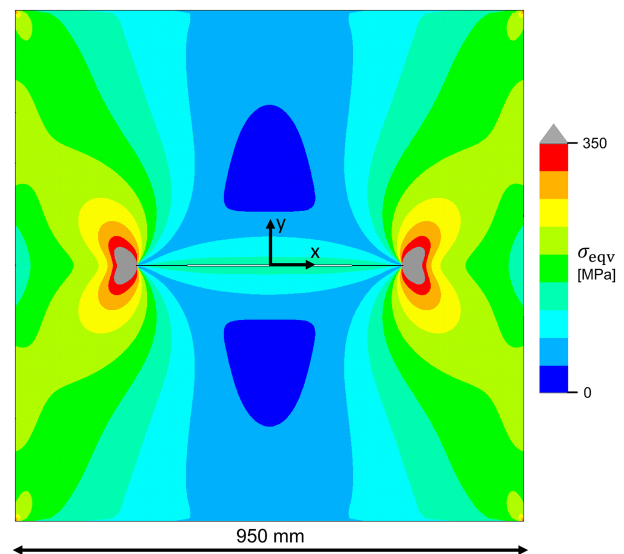


FIGURE 6 Elastic-plastic simulation results for a crack with a length of $a = 250$ mm showing von Mises equivalent stress σ_{eqv} at the maximum nominal load of 120 MPa. The colour bar is limited to $R_{p0.2} = 350 \text{ MPa}$ to reveal the primary plastic zone (grey) [Colour figure can be viewed at [wileyonlinelibrary.com](https://onlinelibrary.com)]

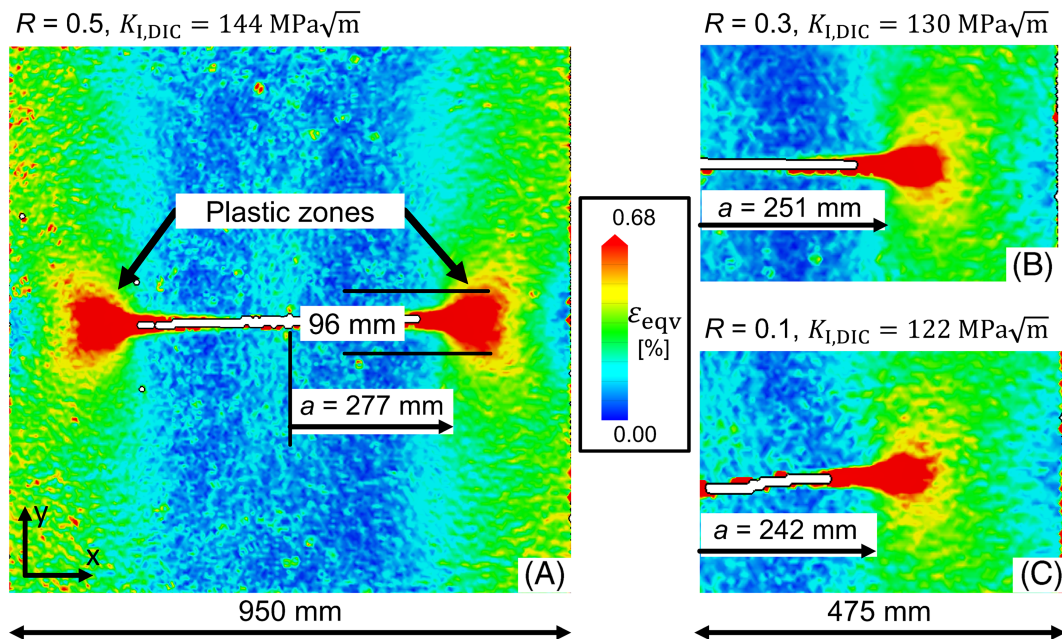


FIGURE 7 Equivalent von Mises strain, ε_v , fields determined by digital image correlation (DIC) at maximum loading conditions for the three experiments right before the final fracture. The plastic zones are shown in red based on the range of the colour scale bar. The load cycles are about 36.6×10^3 , 21.2×10^3 and 17.2×10^3 for A to C, respectively. The load direction is vertical [Colour figure can be viewed at wileyonlinelibrary.com]

3.3 | Fatigue crack propagation data

The da/dN - ΔK FCG curves are shown in Figure 8A. While da/dN is based on continuous potential drop measurements, ΔK is derived from the FEA (square symbols) and DIC (star symbols) results. There are fewer data points for the DIC results because of the limited amount of data. Curves start at a crack propagation rate between 10^{-4} and 10^{-3} mm/cycle and stress intensity factors of about 10 to 20 $\text{MPa}\sqrt{\text{m}}$. The highest crack propagation rates and cyclic stress intensity factors of 4 mm/cycle and 115 $\text{MPa}\sqrt{\text{m}}$, respectively, were reached for the specimen with $R = 0.1$ load ratio. The FCG curves for load ratios $R = 0.3$ and $R = 0.5$ are shifted to the left because of their lower cyclic stress intensity factors.

3.4 | Fractography

Fracture surfaces were investigated to reveal the fracture mechanisms and possible crack closure effects that could be expected up to load ratios $R \leq 0.7$ for AA2024.³⁵ For the first 100 mm of the crack propagation, the specimen with $R = 0.1$ presented a V fracture mode (double shear), as shown in Figure 8B. Then, the fracture mode transitioned to a 45° slant or S-mode (Figure 8C). This transition is characterized by an apparent increased crack propagation rate for the linear-elastic FEA solution

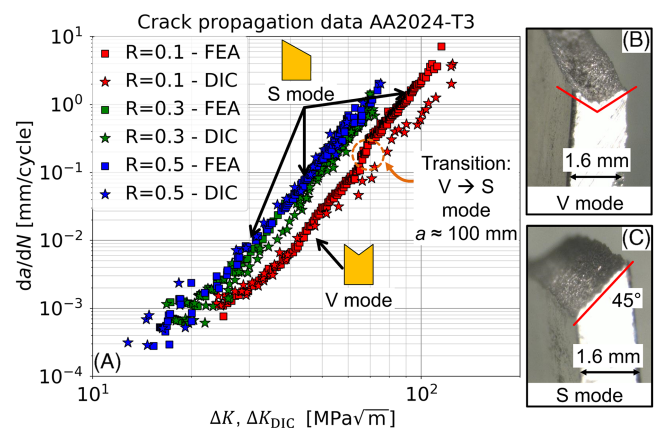


FIGURE 8 (A) Crack propagation data and (B and C) S and V fracture modes observed for experiments with $R = 0.1$. The S mode fracture is representative for $R = 0.3$ and 0.5 . ΔK was calculated with a linear-elastic solution and with a DIC postprocessor based on the interaction integral [Colour figure can be viewed at wileyonlinelibrary.com]

(region indicated by a circle). The corresponding values for K_I are calculated for a flat fracture surface normal to the applied load, and it increases steadily for longer cracks (Figure 5). No change in the slope of the FCG rate is observable for the DIC solution. The DIC and FEA results practically overlap until the V-S transition occurs; higher ΔK values were obtained in DIC postprocessing during the phase when the S-mode fracture is active. The

fracture surfaces for the $R = 0.3$ and $R = 0.5$ experiments had a 45° S-mode from the beginning. The crack propagation curves for these load conditions overlap within a small scatter band.

4 | DISCUSSIONS

Cyclic stress intensity factors greater than $115 \text{ MPa}\sqrt{\text{m}}$ with crack propagation rates up to 4 mm/cycle were achieved for large and thin ($1,250 \times 950 \times 1.6 \text{ mm}^3$) specimens of AA2024-T3 investigated in this study. The crack propagation curves (Figure 8) start at about 10 to $20 \text{ MPa}\sqrt{\text{m}}$, where most FCG results in the literature end. The achieved high-stress conditions are close to crack resistance curve experiments.¹³ We suggest that they may be interpreted as a type of cyclic R-curves. Furthermore, the load cycles between 17×10^3 and 36×10^3 in the experiments are typical magnitudes relevant for commercial aircrafts.³⁶

4.1 | Simulations and experiments

The experimental determination of the PPZ at the crack tip using the DIC system is in good agreement with the simulations. The shapes and extensions are considerably similar with respect to the local spatial resolution of the DIC measurements. A comparison of the PPZs shown in Figure 7 with the simulations in Figure 5 reveals that the elastic-plastic finite element model can predict their size and shape very well. The effect of the plastic wake from the propagating crack is an inherent part of DIC results; however, it cannot be revealed separately as it is not possible to distinguish between elastic and plastic strains without further assumptions. In addition, Figures 6 and 7A show that the limited specimen length and long crack result in a large stress dead zone with reduced stresses/strains (blue) in the centre of the specimen.²³ This fact is well-captured in the simulation model for the linear-elastic calculations of the stress intensity factors. Furthermore, the stress intensity factors determined by the linear-elastic finite element simulations and the DIC postprocessor are in good agreement with each other. Path-independent contour integrals in the linear-elastic DIC field outside the plastic zone can capture the local crack tip loadings without complex elastic-plastic stress-strain parameters. This indicates that the K concept of linear-elastic fracture mechanics can be extended for the case of LSY conditions, which goes far beyond its original definition, that is, plastic zones should be small compared with the crack length. Nevertheless, an overlap of all FCG curves obtained by DIC and potential drop

measurements was expected as they incorporate the effective cyclic stress intensity factors considering intrinsic and extrinsic effects.²⁰ This deviation can be attributed to the macroscopic topology of the fracture surfaces indicated in Figure 8B,C, that is, the differences between V and S modes, and therefore, the complex interaction between the fracture surfaces.

The investigation of the fast FCG rates and large plastic zone sizes obtained in the present work undoubtedly require the use of large specimen sizes. Standard fracture mechanical specimens such as CT75 or MT160 would rapidly fail because of unstable crack growth in regime C (fast crack growth regime). Considering this, the maximum possible crack propagation rates depend on the combination of specimen size and plastic zone expansion. The FCG curves in Figure 8 show a stable crack extension and can therefore be fitted by the Paris Law in the double-logarithmic diagram for numerical predictions of crack growth. Furthermore, the increase in crack propagation rates with load ratio R is in agreement with the literature despite the high crack tip loads.³⁷

4.2 | Fracture modes and crack closure

A predominant 45° shear (S-mode) crack was present for the $R = 0.3$ and $R = 0.5$ specimens, which is typical for high plasticity at the crack tip.³⁸ For the $R = 0.1$ specimen, the transition from the V to the S mode occurred without any observable preindication during the experiment. Figure 9 provides an overview of fracture surfaces before (A and B) and after (C and D) this transition; no fatigue striations are visible on the fracture surfaces. Figure 9A shows a predominantly ductile fracture with tear ridges, ductile dimples and transgranular fracture (1), which are typical for regime C FCG.¹⁰ Furthermore, Figure 9B reveals broken primary intermetallic particles found throughout the fracture surface (2). Thus, the high-load FCG shows evidence of cyclic ductile stable rupture rather than fatigue striations, which should be predominant in regime B (Paris regime) crack propagation. The scanning electron microscope (SEM) micrograph in Figure 9C reveals that there was a relative movement of the S-mode fracture surfaces against each other, that means flattened areas (3) indicate physical contact of the fracture surfaces during crack propagation. Figure 9D shows scratches (marked as (4)) perpendicular to the crack growth direction (black arrow). The concept for the mode I crack closure in the classical sense indicates that forces are transmitted perpendicular to the fracture surfaces when they are in contact.³⁹ This is still possible in the V mode because of the interlocking of the fracture surfaces. In contrast, the surface contact for the

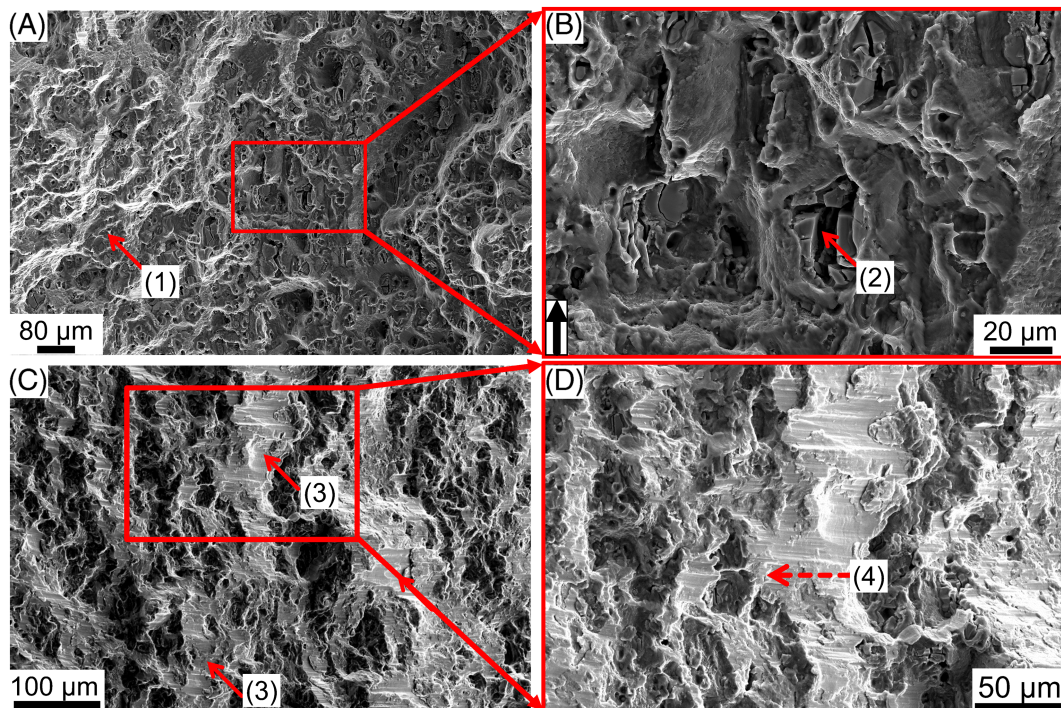


FIGURE 9 Scanning electron microscope (SEM) micrographs of the $R = 0.1$ specimen before and after transition from the V to the S mode. The black arrow indicates the crack growth direction. (A) and (B) show the fracture surface of the V mode at a crack length of 90 mm and $K_{I,max} = 68 \text{ MPa}\sqrt{\text{m}}$. (C and D) Fracture surfaces of the 45° shear S mode at a crack length of 110 mm and $K_{I,max} = 77 \text{ MPa}\sqrt{\text{m}}$ [Colour figure can be viewed at wileyonlinelibrary.com]

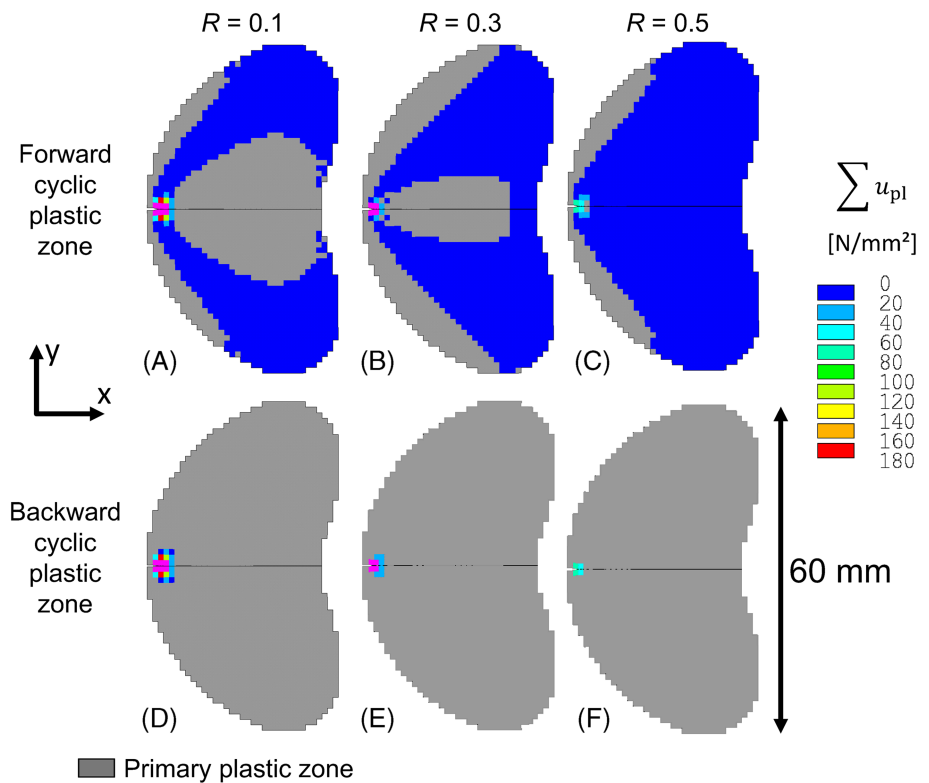
S mode is more complex, as in-plane relative movements are possible in the 45° direction. Therefore, sliding of the 45° fracture surfaces against each other could locally cause additional mode II (in-plane shear) and mode III (out-of-plane shear) loads at the crack front, thereby leading to very complex stress states that can increase crack propagation rates. The simulation model can only represent a straight crack front perpendicular to the load direction. Under these conditions, the DIC-based results consider the complex stress states directly at the crack tip and provide a more accurate solution for the apparently increased ΔK_{DIC} . Thus, the $da/dN - \Delta K_{DIC}$ curve continues almost linearly in the double-logarithmic plot. Physical contact of the fracture surface cannot be observed for the specimen with higher load ratios ($R = 0.3$ and 0.5) as the scratches perpendicular to the crack growth direction are not visible. Thus, the crack propagation curves are very close for these load ratios.

4.3 | Cyclic plastic zone

The highest stress intensity factor reached was $K_{I,max} = 144 \text{ MPa}\sqrt{\text{m}}$, and it was obtained for the $R = 0.5$ specimen because the longest crack length was achieved for this load ratio. The $R = 0.1$ specimen

showed the highest ΔK ($115 \text{ MPa}\sqrt{\text{m}}$) because of the larger crack opening displacements. Effects causing the earlier final fractures at lower load ratios (final crack lengths $a = 277$, 251 and 242 mm for $R = 0.5$, 0.3 and 0.1 , respectively) were not identified at the fracture surfaces. Originally, it was expected that the final fracture would occur at similar crack lengths because of identical PPZ extensions, that is, via plastic collapse or ductile tearing, with respect to the maximum K . Therefore, representative simulations of the cyclic plastic zone were conducted with identical PPZ sizes. To this end, 30 load cycles were simulated until the geometrical extension of the cyclic plastic zone converged. Different types of the cyclic plasticity in the vicinity of the crack tip, namely the forward and backward cyclic plastic zones, are plotted for a crack length of $a = 200$ mm in terms of accumulated plastic strain energy density $\sum u_{pl}$ in Figure 10. This comparison does not include crack propagation in the simulation models as only the effect of energy accumulation in the plastic zone needs to be separated. Lower load ratios should increase the accumulated energy because higher external work is introduced because of the higher load amplitudes ($W = \int F \cdot ds$, where W , F and ds are the work, force and infinitesimal displacement, respectively). The PPZ is plotted in grey; its extension is constant during cyclic loading. The size

FIGURE 10 Finite element analysis (FEA) results of the cyclic plastic zone obtained for a crack length $a = 200$ mm and $K_{I,max} = 107$ MPa \sqrt{m} after 30 load cycles. The colour plot shows the accumulated plastic strain energy density of the forward and backward cyclic plastic zones, while the extension of the primary plastic zone is indicated in grey [Colour figure can be viewed at wileyonlinelibrary.com]



of the forward cyclic plastic zone increases with increasing load ratio while that of the backward cyclic plastic zone decreases. Moreover, the energy accumulation close to the crack tip decreases with increasing load ratio, and it is associated with a higher dislocation movement.⁴⁰ In other words, the work-hardening increases with decreasing load ratio and, therefore, the final unstable rupture occurs at lower crack lengths.

5 | SUMMARY AND CONCLUSIONS

Results of the crack propagation experiments showed that computationally efficient methods based on linear-elastic fracture mechanics can be used to calculate the stress intensity factors in the case of LSY, and they can be applied to crack growth simulations and lifetime predictions for aircraft fuselage skin sections. These data are also relevant to evaluate the damage tolerance of such structures. The fatigue experiments, together with the combination of DIC with linear-elastic as well as elastic-plastic finite element simulations, lead to the following conclusions:

1. Crack propagation starts at rates between 10^{-4} and 10^{-3} mm/cycle and stress intensity factors of about 10 to 20 MPa \sqrt{m} . The highest crack propagation rates and cyclic stress intensity factors of 4 mm/cycle and 115 MPa \sqrt{m} , respectively, were reached for the specimen with $R = 0.1$.
2. The estimation of the stress intensity factors by means of DIC and FEA linear-elastic solutions show similar results even for large plastic deformations, that is, plastic zone extensions up to about 100 mm in the vicinity of the crack tip.
3. The fatigue cracks at $\Delta K > 30$ MPa \sqrt{m} tend to a 45° shear fracture (S mode) with ductile micro-fracture features indicating cyclic tearing. A transition from the V to S fracture mode was observed at a crack length a of approximately 100 mm for the $R = 0.1$ loading condition that resulted in an apparent increase in the FCG rates. Consequently, the FCG diagrams deviated with respect to ΔK based on the linear-elastic solution and the DIC results. This effect may arise because only the DIC calculation can capture the complex loading condition caused by the transition of the fracture mode.
4. The size of the forward cyclic plastic zone increases with an increasing R -ratio while that of the backward cyclic plastic zone decreases. In contrast, the energy accumulation directly at the crack front increases with decreasing load ratio. Therefore, the unstable failure that leads to shorter crack lengths at lower load ratios can be attributed to the increase in the amount of work-hardening at the front of the crack tip.

ACKNOWLEDGEMENT

This work was supported by the German Federal Ministry for Economic Affairs and Energy (BMWi). The

authors would like to thank Julian Schwinn and Dirk Lütz for conducting and supporting the experimental investigations. Open access funding enabled and organized by Projekt DEAL.

AUTHOR CONTRIBUTIONS

All people who meet authorship criteria are listed as authors, and all authors certify that they have participated sufficiently in the work to take public responsibility for the content, including participation in the concept, design, analysis, writing or revision of the manuscript.

NOMENCLATURE

a	crack length
da/dN	crack growth rate
DIC	digital image correlation
ds	infinitesimal displacement
E	Young's modulus
F	force
FCG	fatigue crack growth
FEA	finite element analysis
J	J integral
K_i	stress intensity factors with i for Modes I, II and III
LSY	large-scale yielding
PPZ	primary plastic zone
r_p	primary plastic zone size
R	load ratio
t	time
u_{pl}	plastic strain energy density
ν	Poisson ratio
W	work
ϵ_{total}	total strain
$\epsilon_{elastic}$	elastic strain
$\epsilon_{plastic}$	plastic strain
σ_{yield}	yield strength
$R_{p0.2}$	
σ	stress
ΔK	cyclic stress intensity factor

ORCID

Eric Breitharth  <https://orcid.org/0000-0002-3479-9143>

REFERENCES

- Jones R. Fatigue crack growth and damage tolerance. *Fatigue Fract Eng Mater Struct*. 2014;37(5):463-483.
- Tavares SMO, de Castro PMST. An overview of fatigue in aircraft structures. *Fatigue Fract Eng Mater Struct*. 2017;40(10):1510-1529.
- Schijve J. Fatigue of structures and materials in the 20th century and the state of the art. *Int J Fatigue*. 2003;25(8):679-702.
- Dowling N. Geometry effects and the J-integral approach to elastic-plastic fatigue crack growth. In: Swedlow J, Williams M, eds. *Cracks and Fracture*. West Conshohocken, PA: ASTM International; 1976:19-32.
- Dowling N, Begley J. Fatigue crack growth during gross plasticity and the J-integral. In: Rice J, Paris P, eds. *Mechanics of Crack Growth*. West Conshohocken, PA: ASTM International; 1976:82-103.
- Newman JC, Walker KF. Fatigue-crack growth in two aluminum alloys and crack-closure analyses under constant-amplitude and spectrum loading. *Theor Appl Fract Mech*. 2019;100:307-318.
- Donald K, Paul CP. An evaluation of Delta Keff estimation procedures on 6061-T6 and 2024-T3 aluminum alloys. *Int J Fatigue*. 1999;21:47-57.
- Ghidini T, Donne CD. Fatigue crack propagation assessment based on residual stresses obtained through cut-compliance technique. *Fatigue Fract Eng Mater Struct*. 2007;30(3):214-222.
- Liu A, Allison J, Dittmer D, Yamane J. Effect of biaxial stresses on crack growth. In: Smith C, ed. *Fracture Mechanics: Proceedings of the Eleventh National Symposium on Fracture Mechanics: Part I*. West Conshohocken, PA: ASTM International; 1979:5-22.
- Ritchie R. Mechanisms of fatigue-crack propagation in ductile and brittle solids. *Int J Fract*. 1999;100(1):55-83.
- Paul SK, Tarafder S. Cyclic plastic deformation response at fatigue crack tips. *Int J Press Vessel Pip*. 2013;101:81-90.
- Memhard D, Brocks W, Fricke S. Characterization of ductile tearing resistance by energy dissipation rate. *Fatigue Fract Eng Mater Struct*. 1993;16(10):1109-1124.
- Schwalbe K-H, Setz W. R curve and fracture toughness of thin sheet materials. *J Test Eval*. 1981;9:182-194.
- Schwalbe H. R-curve testing and its relevance to structural assessment. *Fatigue Fract Eng Mater Struct*. 1998;21:1259-1271.
- Lu L, Wang S. Relationship between crack growth resistance curves and critical CTOA. *Eng Fract Mech*. 2017;173:146-156.
- Roux S, Réthoré J, Hild F. Digital image correlation and fracture: an advanced technique for estimating stress intensity factors of 2D and 3D cracks. *J Phys D Appl Phys*. 2009;42(21):214004.
- Tong J. Full-field characterisation of crack tip deformation and fatigue crack growth using digital image correlation—a review. *Fatigue Fract Eng Mater Struct*. 2018;41(9):1855-1869.
- Mokhtarshirazabad M, Lopez-Crespo P, Zanganeh M. Stress intensity factor monitoring under cyclic loading by digital image correlation. *Fatigue Fract Eng Mater Struct*. 2018;41:2162-2171.
- Christopher CJ, James MN, Patterson EA, Tee KF. A quantitative evaluation of fatigue crack shielding forces using photoelasticity. *Eng Fract Mech*. 2008;75(14):4190-4199.
- González GLG, González JAO, Castro JTP, Freire JLF. A J-integral approach using digital image correlation for evaluating stress intensity factors in fatigue cracks with closure effects. *Theor Appl Fract Mech*. 2017;90:14-21.
- Réthoré J, Gravouil A, Morestin F, Combescure A. Estimation of mixed-mode stress intensity factors using digital image correlation and an interaction integral. *Int J Fract*. 2005;132(1):65-79.
- Becker TH, Mostafavi M, Tait RB, Marrow TJ. An approach to calculate the J -integral by digital image correlation displacement field measurement. *Fatigue Fract Eng Mater Struct*. 2012;35(10):971-984.

23. Farahani BV, Eslami S, de Melo FQ, Tavares PJ, Moreira PMGP. Concept of stress dead zone in cracked plates: theoretical, experimental, and computational studies. *Fatigue Fract Eng Mater Struct*. 2019;42(11):2457-2467.
24. Mathieu F, Hild F, Roux S. Identification of a crack propagation law by digital image correlation. *Int J Fatigue*. 2012;36(1):146-154.
25. Vasco-Olmo JM, Díaz Garrido FA, Antunes FV, James MN. Plastic CTOD as fatigue crack growth characterising parameter in 2024-T3 and 7050-T6 aluminium alloys using DIC. *Fatigue Fract Eng Mater Struct*. 2020;43(8):1719-1730.
26. Vormwald M, Hos Y, Freire JLF, Gonzáles GLG, Díaz JG. Crack tip displacement fields measured by digital image correlation for evaluating variable mode-mixity during fatigue crack growth. *Int J Fatigue*. 2018;115:53-66.
27. Schwalbe K-H, Hellmann D. Application of the electrical potential method to crack length measurements using Johnson's formula. *J Test Eval*. 1981;9:218-220.
28. Kuna M. *Finite Elements in Fracture Mechanics*. Dordrecht: Springer Netherlands; 2013. <https://doi.org/10.1007/978-94-007-6680-8>
29. Stern M, Becker EB, Dunham RS. A contour integral computation of mixed-mode stress intensity factors. *Int J Fract*. 1976;12:359-368.
30. Breitbarth E, Strohmann T, Besel M, Reh S. Determination of stress intensity factors and J integral based on digital image correlation. *Frat Ed Integrità Strutt*. 2019;13(49):12-25.
31. ANSYS. Theory Reference Manual, Release 19.1.
32. Breitbarth E, Besel M. Energy based analysis of crack tip plastic zone of AA2024-T3 under cyclic loading. *Int J Fatigue*. 2017;100:263-273.
33. Irwin GR. Onset of fast crack propagation in high strength steel and aluminum alloys. *Sagamore Res Conf Proc*. 1956;2:289-305.
34. Shrivastava S, Ghosh C, Jonas JJ. A comparison of the von Mises and Hencky equivalent strains for use in simple shear experiments. *Philos Mag*. 2012;92(7):779-786.
35. Elber W. The significance of fatigue crack closure. In: Rosenfeld M, ed. *Damage Tolerance in Aircraft Structures*. West Conshohocken, PA: ASTM International; 1971:230-242.
36. Schijve J. Fatigue of aircraft materials and structures. *Int J Fatigue*. 1994;16(1):21-32.
37. Huang X, Moan T. Improved modeling of the effect of R-ratio on crack growth rate. *Int J Fatigue*. 2007;29(4):591-602.
38. Schijve J. Shear lips on fatigue fractures in aluminium alloy sheet material. *Eng Fract Mech*. 1981;14(4):789-800.
39. Pippin R, Hohenwarter A. Fatigue crack closure: a review of the physical phenomena. *Fatigue Fract Eng Mater Struct*. 2017;40(4):471-495.
40. Breitbarth E, Zaefferer S, Archie F, Besel M, Raabe D, Requena G. Evolution of dislocation patterns inside the plastic zone introduced by fatigue in an aged aluminium alloy AA2024-T3. *Mater Sci Eng A*. 2018;718:345-349.

SUPPORTING INFORMATION

Additional supporting information may be found online in the Supporting Information section at the end of this article.

How to cite this article: Breitbarth E, Strohmann T, Requena G. High-stress fatigue crack propagation in thin AA2024-T3 sheet material. *Fatigue Fract Eng Mater Struct*. 2020;43:2683-2693. <https://doi.org/10.1111/ffe.13335>